

SCILLA: SurfaCe Implicit Learning for Large urban Area, a volumetric hybrid solution

Hala Djeghim^{1,2} Nathan Piasco¹ Moussab Bennehar¹ Luis Roldão¹
 Dzmitry Tsishkou¹ Désiré Sidibé²
¹Noah’s Ark, Huawei Paris Research Center, France
²IBISC, Evry Paris-Saclay University, France

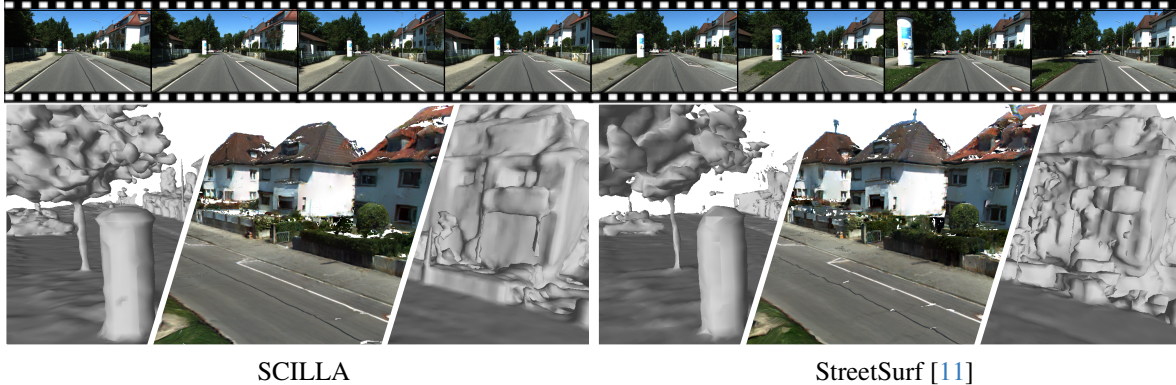


Figure 1. We introduce **SCILLA**, a novel hybrid implicit learning method capable to accurately reconstruct large driving scenes from 2D RGB input images solely. Extensive experiments on four popular driving datasets show the superiority of SCILLA’s mesh (left) over previous state-of-the-art methods such as StreetSurf [11] (right). Figure shows both original and textured mesh obtained from both methods.

Abstract

Neural implicit surface representation methods have recently shown impressive 3D reconstruction results. However, existing solutions struggle to reconstruct driving scenes due to their large, unbounded, and highly complex nature. Hence, to achieve accurate reconstructions, additional supervision data such as LiDAR, strong geometric priors, and long training times are required. To tackle such limitations, we present **SCILLA**, a new hybrid implicit surface learning method to reconstruct large driving scenes from 2D images. **SCILLA**’s hybrid architecture models two separate implicit fields: one representing the volumetric density of the scene, and another one representing the signed distance to the surface. To accurately reconstruct urban outdoor driving scenarios, we introduce a novel volume-rendering strategy that relies on self-supervised probabilistic density estimation to sample points near the surface and transition progressively from volumetric to surface representation. Our solution permits a proper and fast initialization of the signed distance field without relying on any geometric prior on the scene, compared to concurrent methods. By conducting extensive ex-

periments on four outdoor driving datasets, we show that **SCILLA** can learn an accurate and detailed 3D surface scene representation in various driving scenarios while being two times faster to train compared to previous state-of-the-art solutions.

1. Introduction

Achieving accurate 3D reconstruction from multi-view-consistent images has been an important topic in computer vision and computer graphics communities for decades. A 3D representation of the perceived environment is fundamental for many tasks, such as scene re-lighting [44], scene editing [45] and 3D object insertion for artificial data augmentation [39].

Recently, neural implicit surface representation methods [37, 42] have shown impressive 3D surface reconstruction performance from monocular images, achieving highly detailed and precise mesh representations. Such methods are originally inspired by Neural Radiance Fields (NeRF) [23], and re-framed for multi-view surface reconstruction. NeRF introduced volume rendering for Novel View Synthesis (NVS) by sampling points along camera

rays. These points, along with their viewing directions, are fed into a Multi-Layer Perceptron (MLP) to predict their respective colors and densities. The final image is rendered by blending these predicted values using alpha compositing. Conversely, neural surface representation methods aim to approximate the surface using a learnable Signed Distance Function (SDF) [37, 42]. Unlike NeRF, the outputs of the MLP are colors and SDF values instead of colors and volumetric densities, which are later blended using a modified alpha-compositing equation adapted to SDF. An accurately reconstructed surface is represented as a zero-level set of the SDF. Assuming the objects lying at the center of the scene, the SDF is first initialized to form a spherical shape to bound the region of interest. Although current methods achieve impressive reconstruction results, they are mostly applied to simple, bounded and object-centric or landmarks scenes. Applying such methods to unbounded driving scenarios results in sub-optimal reconstruction given their significantly different nature. To overcome such limitations, implicit surface reconstruction of large outdoor driving scenes commonly relies on LiDAR supervision [27, 39] or strong geometric priors [11]. These approaches require longer training time to produce qualitative outdoor scene reconstruction meshes from 2D images.

To address those challenges, we propose SCILLA, a hybrid approach to accurately initialize a signed distance field of an unbounded area and represent complex surfaces from urban outdoor driving scenarios with high accuracy and geometric precision, while requiring half of the training time compared to other state-of-the-art solutions such as Street-Surf [11]. We propose a hybrid architecture that models two separate implicit fields: one representing the volumetric density of the scene and another one representing the signed distance to the surface. SCILLA’s novel volume rendering approach relies on a self-supervised density estimator which permits to sample points near the surface along with a progressive sampling strategy that smoothly initializes and transitions from a volumetric to a surface representation, drastically reducing the model convergence time. Inspired by previous state-of-the-art works [11, 43], we supervise surface normals by relying on normal cues predicted from a pre-trained monocular estimator [8]. We extensively validate our solution on KITTI-360 [20], Pandaset [41], Waymo Open Dataset [32], and nuScenes [3]. By comparing the quality of the extracted meshes from the signed distance field, we show that our method can efficiently reconstruct urban outdoor scenarios showing SoTA accuracy. To summarize, the main contributions of our work are:

- A novel implicit hybrid learning method to progressively initialize the signed distance field for surface reconstruction on large outdoor driving scenes,
- A hybrid architecture that models two distinct implicit fields to represent both the volumetric density and the

signed distance field,

- A new volume rendering technique that relies on self-supervised probabilistic density estimation to efficiently sample points near the surface and smoothly transition from a volumetric representation to a surface representation, significantly reducing training times,
- Various regularization techniques of the signed distance field to enhance our model’s implicit surface representation learning and convergence are presented.

2. Related work

Multi-view surface reconstruction. Traditional surface reconstruction techniques represent a scene either by occupancy grids [7, 26, 34, 35] or relying on point clouds [9, 28, 29, 31]. Occupancy grids-based methods are often limited by the voxel resolution and suffer from high memory consumption. On the other hand, Multi-View Stereo (MVS) techniques [24] generate, from posed images, dense point clouds associated with surface normal that can be utilized in a subsequent surface reconstruction step [16]. These methods heavily depend on the quality of the generated point cloud. Nevertheless, they can accumulate errors due to their complex multi-step pipelines, and are mostly designed for object-centric scenes with high overlaps between the observations. We refer the reader to dedicated surveys for in-depth analysis of such techniques [2, 22, 46].

Neural implicit surface representations. NeRF-based methods can achieve impressive NVS results but fail to accurately reconstruct scene surfaces given the lack of constraints or priors on the surface when modelling the scene as a density volume. Neural surface reconstruction approaches on the other hand, explicitly represent the surface as an SDF and propose various adaptations to train such methods through differentiable volume rendering [37, 42]. NeuS [37] proposes a novel SDF-based rendering equation that relies on SDF values to compute the alpha blending factor used in volume rendering instead of densities as presented in the original NeRF [23]. Nevertheless, NeuS’s original contribution is designed mainly for object-centric datasets and requires a long training time. Some recent works aim to reduce the training time [38] or reconstruct large-scale highly detailed landmark scenes [19]. However, such approaches are not tailored for large unbounded driving scenarios and still require hours of training. In contrast, our method is built upon NeuS’s formulation and it is designed to reliably represent urban outdoor driving scenes.

Urban outdoor surface reconstruction. Urban outdoor scene reconstruction is one of the main subjects contributing to resolving many downstream applications, such as inverse rendering and object insertion [39]. Latest SoTA

approaches rely on SDF-based surface reconstruction for urban outdoor scenes, to disentangle the scene’s geometry from other scene parameters. Neuralangelo [19], a SoTA method for outdoor landmarks reconstruction, requires many overlapping images and the region of interest of the scene to be bounded to initialize the SDF with a spherical shape. Few methods consider acquisition from a moving camera rig for driving sequences surface reconstruction. Existing solutions are mainly guided by LiDAR such as FEGR [39] and Urban Radiance Fields [27], limiting their large-scale deployment. StreetSurf [11], the most related method to our proposal, presents a solution that disentangles close-range view from distant-range view, alongside a signed distance field initialization technique to match the road surface according to the ego poses of the vehicle. This surface initialization approach is rough, not straightforward, and heavily depends on the ego poses and the assumption that the road and the sidewalk are at the same height in every part of the scene. Additionally, StreetSurf relies on the assumption that self-driving scenes are mostly long and narrow and showcase reconstruction of the scene from only one public dataset (i.e. Waymo Open Dataset [32]). In reality, driving datasets frequently contain scenarios where the scenes are short and curvy, hence, disentangling the close and far range in those situations becomes more challenging. Instead, our solution is more adaptive in comparison to StreetSurf as it does not rely on strong assumptions about the scene’s topology. Furthermore, SCILLA is also more compact and faster to train as the entire scene is represented by a single hybrid implicit field.

Hybrid scene representation. Some SoTA methods have already investigated the use of hybrid rendering solutions relying on both volumetric and surface composing. Wang et al. [40] introduced a hybrid rendering method based on NeuS [37] that uses a spatially varying kernel, which changes according to the fuzziness of the surface. Based on the kernel, a narrow mesh envelope is extracted around the surface, which then enables ray casting only inside this envelope. This solution helps accelerate both rendering time and quality. Other methods [12, 14, 33] focus on a hybrid representation that both relies on an explicit representation (meshes) and an SDF representation. The hybrid volume-mesh representation enables efficient rendering and less resourceful storage while outputting an implicit geometrical representation. In addition to fast training times, this representation also benefits from easy integration into computer graphics engines. NeuSG [5] combines 3D Gaussian Splatting [17] with NeuS to obtain an accurate Gaussian cloud close to the surface that serves as a direct supervision signal during NeuS training. The aforementioned solutions mainly focus on improving the rendering speed and are better fitted for small scenes with a hybrid representation. In our

proposal, we jointly train a hybrid model to benefit from the fast training of a density-based approach along with an accurate geometric representation obtained thanks to the signed distance field learning.

3. Method

SCILLA models the volumetric density and signed distance field in a hybrid architecture. The details of this architecture are presented in Sec. 3.2, while the novel underlying volume rendering strategy is explained in Sec. 3.3. Our hybrid strategy relies on a self-supervised density distribution estimation to sample points near the surface and progressively transition from a volumetric to an implicit surface representation. To facilitate the convergence of our method, we further introduce regularization techniques for the signed distance field. The overall architecture of our proposed method is illustrated in Fig. 2.

3.1. Preliminaries

NeRF’s Implicit Volumetric Representation. NeRF [23] takes as input the 3D positions $x_i \in \mathbb{R}^3$ and the viewing direction $d \in \mathbb{R}^2$ of sampled points along each camera ray r and predicts their corresponding densities $\sigma_i \in \mathbb{R}$ and colors $c_i \in \mathbb{R}^3$. This representation of the scene is approximated using a Multi-Layer Perceptron (MLP). Finally, volume rendering is used to alpha-composite the colors of the samples along each ray and render the final pixel color $\hat{C}(r) \in \mathbb{R}^3$:

$$\hat{C}(r) = \sum_{i=1}^N w_i c_i, \quad w_i = T_i \alpha_i, \quad (1)$$

where $T_i = \prod_{j=1}^{i-1} (1 - \alpha_j)$ is the accumulated transmittance along the ray and $\alpha_i \in \mathbb{R}$ a blending factor. This factor (referred to in the literature as the alpha-value) is used for alpha-composing, and is given by:

$$\alpha_i = 1 - \exp(-\sigma_i \delta_i), \quad (2)$$

with $\delta_i \in \mathbb{R}$ being the distance between the samples along the ray. Note that in SCILLA’s hybrid formulation, we refer to this value as α_i^v to disambiguate from alpha values derived from the estimated SDF which is introduced in Eq. 3.

SDF representation with NeuS. For an accurate surface-based representation of a 3D scene, NeuS [37] presented a different formulation of the NeRF’s volume rendering equation. They represent the scene as a signed distance function, where the surface is the zero-level set of such function: $S = \{x \in \mathbb{R}^3 | f(x) = 0\}$, where $f(x)$ is the signed distance value at a given position x . NeuS adopts a volume rendering formulation introducing a density distribution function which is formulated as the derivative of the

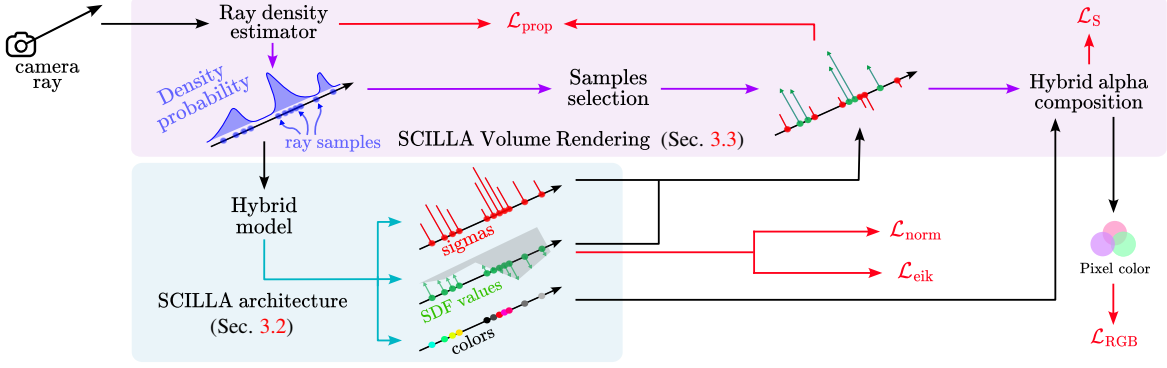


Figure 2. **SCILLA overview** – Our solution can be divided into two key components: an hybrid scene representation (Sec. 3.2) and a ray-based volumetric rendering that progressively transitions from density to SDF sample alpha composition (Sec. 3.3).

sigmoid function $\Phi_s(x) = (1 + e^{-sx})^{-1}$, that is: $\phi_s(x) = se^{-sx}/(1+e^{-sx})^2$. The standard deviation of ϕ_s is $1/s$ and, as the network converges to an accurate surface representation, this parameter moves toward zero. Following NeuS’s formulation, the volumetric alpha used in Eq. 1 is replaced by the following equation to approximate the color $\hat{C}(r)$:

$$\alpha_i = \max\left(\frac{\Phi_s(f(p_i)) - \Phi_s(f(p_{i+1}))}{\Phi_s(f(p_i))}, 0\right), \quad (3)$$

where $f(p_i)$ and $f(p_{i+1})$ are signed distance values at section points centered on x_i . In our formulation, we denote alpha values derived from the estimated SDF as α_i^f .

3.2. SCILLA’s hybrid architecture

Unlike SoTA methods that singularly represent either a density or an SDF field, our hybrid method SCILLA learns the two different fields simultaneously, as illustrated in Fig. 3. SCILLA expresses the scene using two functions, \mathcal{F}_Θ^h and \mathcal{F}_Θ^c , encoded respectively by two MLPs. The input 3D position x and viewing direction d are embedded respectively via a positional and directional embedding into $\text{emb}_x(x)$ and $\text{emb}_d(d)$.

\mathcal{F}_Θ^h takes as input $\text{emb}_x(x)$ and outputs a density σ , a signed distance value $f(x)$, and a latent vector h , that is $(\sigma, f(x), h) = \mathcal{F}_\Theta^h(\text{emb}_x(x))$.

\mathcal{F}_Θ^c on the other hand takes as input the latent vector h that is outputted by \mathcal{F}_Θ^h in addition to the embedded viewing direction $\text{emb}_d(d)$ and the normal vector \vec{n} obtained from the gradient of the SDF, to predict the color $c = \mathcal{F}_\Theta^c(\text{emb}_d(d), h, \vec{n})$.

3.3. SCILLA’s volume rendering

Probabilistic density estimation. Probabilistic density estimation along the ray is employed for a more targeted sampling strategy that samples fewer points and accelerates the overall method’s training time. Guided by the es-

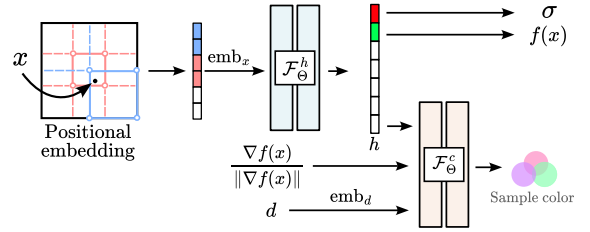


Figure 3. **SCILLA architecture** – Our method uses two MLP functions \mathcal{F}_Θ^h and \mathcal{F}_Θ^c to output SDF values and density (σ and $f(x)$, respectively) along with color values given an input sample. We inspire from NeRF and design \mathcal{F}_Θ^c to output the color given the latent vector h outputted by \mathcal{F}_Θ^h , the viewing direction (d) and the normal vector \vec{n} obtained from the gradient of the SDF.

timated density, N points are sampled along the ray, where higher density indicates the presence of the surface. Using SCILLA’s architecture, alpha values are computed for these samples, and volume rendering is performed to obtain the final color associated with the ray. This resulting color is then compared to the ground truth value to train our model.

$$\hat{C}(r) = \sum_{i=1}^N T_i \alpha_i c_i, \quad (4)$$

$$\text{with } \alpha_i = \begin{cases} \alpha_i^v & \text{if computed from } \sigma_i \text{ (Eq. 2),} \\ \alpha_i^f & \text{if computed from } f(x_i) \text{ (Eq. 3).} \end{cases}$$

The strategy of associating a sample to either a volumetric or surface-based representation is discussed in the next section.

The weights w_i associated with each sample (Eq. 1) serve as a supervision signal to our probabilistic density estimator. Hence, we can refine in a self-supervised manner the prediction of the expected density along the ray. We rely on Mip-NeRF 360’s [1] proposal networks as our volumetric density estimator and use their introduced proposal loss,

$\mathcal{L}_{\text{prop}}$, to refine density estimation from the weights w_i of our main model.

SDF progressive initialization: Volumetric to surface representation. Starting from a pure volumetric density training ($\alpha_i = \alpha_i^v$), we introduce a progressive initialization of the signed distance field, that transitions from a volumetric to an SDF representation. Our approach is based on the premise that estimating the density σ_i at a specific location requires less complex geometric understanding in contrast to estimating the signed distance to the closest point to the surface (i.e. $f(x_i)$). 3D geometry represented as density field contains less information than SDF field: the former contains occupancy information (which can be considered as binary) whereas the latter represents in addition continuous distances to the surface. Therefore, learning a density field is simpler compared to the SDF field (see Fig. 6 of our ablation section). By initially leveraging a pure volumetric density representation during training, we shorten the convergence time of our density estimator.

Our progressive initialization strategy can be outlined as follows:

- **Volumetric stage:** all the samples along the ray express volumetric densities, and their alpha values are computed with σ_i .
- **Hybrid stage:** we gradually assign samples along the ray to train our signed distance field. Within the same ray, a portion of sample values is represented with volumetric alpha α_i^v , while the remainder is computed with α_i^f .
- **Surface stage:** we increase the number of samples for which alpha values are computed using $f(x)$ until we transition to a complete surface representation.

Hybrid stage regularization. Composing alpha values obtained from our two different geometric representations is not straightforward as the learning dynamic of the density and the SDF are not the same. As mentioned earlier, learning a volumetric representation of the scene based only on spatial density is easier and faster to learn compared to learning an arbitrary signed distance field of a complex outdoor scene. To facilitate the convergence of our representation, we introduce two regularization methods: **probability-based sampling attribution** and **SDF-gradient normalization**.

Probability-based samples attribution. To assign the alpha value based on density or SDF to a sample, we initially start with a random selection for each ray. We noticed that this association strategy is not suitable: the signed distance field could not be properly initialized during the hybrid stage. To solve this problem, we introduce a probability-based sample association. We assign α_i^f to samples with the highest predicted density to initialize the signed distance field. It facilitates the learning of the signed distance field by limiting the range of predicted values, as all the points are sampled close to a surface.

SDF-gradient normalization. During the hybrid stage, where α_i^v and α_i^f are jointly composed, we observed that the surface representation tends to predict large SDF gradient values to align α_i^f with α_i^v (we refer to our supplementary materials for further details). To address this, we normalize the SDF gradient in the α_i^f computation to prevent it from compensating for differences in the alpha distribution.

3.4. Optimization

Photometric loss. We use the standard L_1 loss to minimize the pixel-wise color difference between the rendered image \hat{C} , and the ground truth image C , as well as DSSIM [36] loss on color patches.

Monocular cues. As we target to reconstruct outdoor datasets, we add an additional sky loss to our model. Similar to StreetSurf [11], we model the sky color with an auxiliary MLP conditioned on the ray direction and use a loss to constrain the opacity of sky pixels to zero. The segmentation mask is obtained with an off-the-shelf semantic segmentation network [6].

Inspired by MonoSDF[43] and StreetSurf [11], we use off-the-shelf monocular depth estimation models to supervise the rendered normals $\hat{N}(r)$. In standard solutions [11, 43], the monocular normal loss is minimized according to the predicted normal accumulated along the ray:

$$\hat{N}(r) = \sum_{i=1}^N T_i \alpha_i \frac{\nabla f(x_i)}{\|\nabla f(x_i)\|_2}, \quad (5)$$

$$\mathcal{L}_{\hat{N}} = \left\| \hat{N}(r) - \bar{N}(r) \right\| + \left\| 1 - \hat{N}(r)^\top \bar{N}(r) \right\|. \quad (6)$$

In our proposal, however, for more accurate and targeted supervision, we supervise only the normal associated with the closet sample x_N to the surface estimated by transmittance saturation:

$$\mathcal{L}_{\hat{N}} = \left\| \frac{\nabla f(x_N)}{\|\nabla f(x_N)\|_2} - \bar{N}(r) \right\| + \left\| 1 - \left(\frac{\nabla f(x_N)}{\|\nabla f(x_N)\|_2} \right)^\top \bar{N}(r) \right\|. \quad (7)$$

Signed distance field regularization. Similar to [37], to constrain our model to respect the eikonal equation [10] we use the eikonal regularization defined as:

$$\mathcal{L}_{\text{eik}} = \frac{1}{N} \sum_{i=1}^N (\|\nabla f(x_i)\|_2 - 1)^2. \quad (8)$$

According to NeuS formulation of the alpha compositing equation (Eq. 3), the network converges properly when the standard deviation $1/s$ of ϕ_s approaches zero. In complex driving scenarios and very large scenes, the parameter

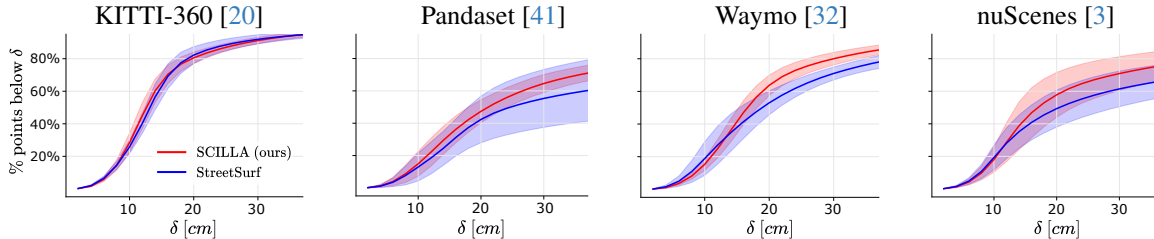


Figure 4. Mean cumulative delta error for both **SCILLA** and **StreetSurf** computed across the four sequences from each dataset as detailed in Tab. 1. Curves indicate the percentage of ground-truth points having an error distance to the closest predicted mesh triangle which is lower than a given value. Light contours represent the standard deviation for each method.

	KITTI-360 [20]								Pandaset [41]							
	Seq. 30		Seq. 31		Seq. 35		Seq. 36		Seq. 23		Seq. 37		Seq. 42		Seq. 43	
	P→M	Prec.	P→M	Prec.	P→M	Prec.	P→M	Prec.	P→M	Prec.	P→M	Prec.	P→M	Prec.	P→M	Prec.
StreetSurf [11]	0.19	0.50	0.15	0.71	0.16	0.67	0.15	0.66	2.35	0.10	0.48	0.4	0.40	0.30	0.28	0.31
SCILLA (ours)	0.18	0.56	0.15	0.71	0.15	0.66	0.16	0.72	0.51	0.23	0.29	0.46	0.36	0.29	0.35	0.34
COLMAP [30]	0.15	0.70	0.12	0.81	0.12	0.78	0.15	0.74	0.71	0.41	1.0	0.52	0.78	0.53	0.28	0.31
OpenMVS [4]	0.13	0.77	0.12	0.80	0.11	0.82	0.13	0.80	0.65	0.56	1.02	0.53	0.74	0.58	0.28	0.31

	Waymo [32]								nuScenes [3]							
	Seq. 10061		Seq. 13196		Seq. 14869		Seq. 102751		Seq. 0034		Seq. 0071		Seq. 0664		Seq. 0916	
	P→M	Prec.	P→M	Prec.	P→M	Prec.	P→M	Prec.	P→M	Prec.	P→M	Prec.	P→M	Prec.	P→M	Prec.
StreetSurf [11]	0.26	0.42	0.37	0.53	0.25	0.35	0.30	0.23	0.93	0.27	0.80	0.47	0.70	0.50	0.67	0.28
SCILLA (ours)	0.23	0.43	0.25	0.48	0.20	0.47	0.24	0.30	0.46	0.20	0.25	0.59	0.44	0.40	0.25	0.54
COLMAP [30]	0.27	0.56	0.78	0.53	0.19	0.67	0.27	0.58	0.67	0.48	0.85	0.67	0.80	0.62	0.80	0.68
OpenMVS [4]	0.3	0.57	0.76	0.53	0.21	0.67	0.24	0.63	0.62	0.51	0.86	0.69	0.76	0.70	0.75	0.69

Table 1. Quantitative results on KITTI-360 [20], Pandaset [41], Waymo Open Dataset [32] and nuScenes [3]. We report the mean Point to Mesh (P→M) distance in meters m , and the percentage of points with a distance to mesh below $0.15m$ (Prec.). We highlight best performing SDF methods in green and MVS methods in blue.

s does not always reach a satisfactory level of convergence. Unlike StreetSurf which manually fixes the parameter s to increment linearly, we introduce a regularization term on s : $\mathcal{L}_s = 1/(s + \epsilon)$.

4. Experiments

We evaluate the performance of SCILLA on multiple driving scenes and provide qualitative and quantitative comparisons compared to relevant methods.

4.1. Implementation details

We use hash encoding to encode the positions [25] (with the same default parameters as in InstantNGP [25]), and spherical harmonics to encode the viewing directions. We use 2 layers with 64 hidden units for the MLPs \mathcal{F}_Θ^h and \mathcal{F}_Θ^c . Pure volumetric stage last for the 100 first steps and the hybrid stage ends at 35% of the total training time. We perform our experiments on a single high-tier GPU using Adam optimizer with a cosine learning rate decay from 10^{-2} to 10^{-4} . For the parameter s , we apply a slightly slower weight decay (10^{-3} to 10^{-5}) to stabilize convergence. We train our model for a total of 14k iterations. Following the literature, we use Marching Cubes [21] to generate the final mesh that represents the scene. Further details on implementation can

be found in the supplementary materials.

4.2. Datasets

We evaluate our method on four public driving datasets: KITTI-360 [20], nuScenes [3], Waymo Open Dataset [32] and Pandaset [41]. We conduct our experiments on four scenes from each dataset. Sequences were selected to have large differences between them. All sequences are static, except for Pandaset where dynamic vehicles are masked during training. Complete details about the selected sequences can be found in our supplementary.

4.3. Baseline

StreetSurf [11] is the current SoTA for surface reconstruction in driving scenes, using road-based surface initialization tailored for such sequences. It employs hierarchical space partitioning with 3 distinct fields to model close-range, far-range, and sky areas, along with 3D and 4D hash grid positional encoding and occupancy grids for efficient ray sampling. We used the official open-source implementation, evaluated with monocular depth supervision, and deactivated trajectory optimization for a fair comparison. All experiments were conducted on the same computational setup. We also extensively tested Neuralangelo [19] on the

selected driving sequences with various training strategies and hyperparameters tuning but did not achieve satisfactory results. Neuralangelo’s need for a bounded scene to initialize the SDF in a sphere shape makes it unsuitable for the open, unbounded nature of driving sequences. Further details can be found in our supplementary materials. For a comprehensive comparison, we benchmark SCILLA’s mesh reconstruction against two classic MVS methods: Delaunay triangulation in COLMAP [30] and mesh reconstruction [15] from OpenMVS [4], both using the denser point cloud from COLMAP.

4.4. Evaluation metrics

To evaluate the quality of the reconstructed surfaces, we report two metrics:

Point to Mesh (P→M): the mean distances from the ground truth LiDAR points to the predicted SDF-generated mesh.

Precision (Prec.): the percentage of LiDAR points with a distance to the mesh below 0.15m.

4.5. Results

Quantitative analysis. We report quantitative results on the 4 datasets in the Tab. 1. Results show that SCILLA achieves on par results with StreetSurf on KITTI-360 dataset, with a mean P→M error of 16 centimeters. However, for the remaining datasets, SCILLA consistently outperforms StreetSurf by achieving lower P→M error and higher precision among most scenes. We attribute similar results on KITTI-360 because of its topology with mainly straight roads and open scenes which are more suitable to the design choices done by StreetSurf. Conversely, the other datasets contain more challenging scenarios with wide, non-straight roads, and a high level of details (we refer to the qualitative analysis). SCILLA shows comparable P→M error to classic MVS methods on KITTI-360, due to KITTI-360’s suitability for multi-view reconstruction, with high-quality images and the large FOV of the vehicle-mounted cameras. However, in more complex environments, SCILLA consistently outperforms MVS methods by achieving lower P→M error. Since they rely on dense point clouds for the final reconstruction, MVS methods can achieve higher precision. Fig. 4 shows the mean cumulative delta error across the four sequences from each dataset for both SDF methods. Our method’s cumulative errors are consistently lower for distances below 40cm. We additionally show the standard deviation of the error computed along all sequences and notice that our errors remain consistent across the different scenes in contrast to StreetSurf. Averaged across the four datasets, SCILLA achieves a mean P→M error of 0.28m, which is nearly half of StreetSurf’s 0.53m, with a mean precision of 0.46% compared to StreetSurf’s 0.42%.

	Total train time (min)	GPU memory (Gb)	Params size (MiB)
StreetSurf [11]	40	19	92.59
SCILLA (ours)	20	8	27
COLMAP [30]	30	<1	–
OpenMVS [4]	30	<1	–

Table 2. **Training analysis.**

Efficiency. We report in Tab. 2 the computational performance of each method. SCILLA uses a single 3D hierarchical hash grid, unlike StreetSurf’s two grids (3D and 4D) [11], making it more efficient with one-third of the parameters and half the GPU memory during training. Additionally, SCILLA requires half the training time per scene compared to StreetSurf.

Qualitative analysis. The quantitative evaluation presented in the previous section (Sec. 4.5) is computed from the accumulated ground-truth LiDAR which is sparse and may miss some scene regions. To complete our evaluation, we present qualitative results in Fig. 8. Results demonstrate that SCILLA reconstructs higher-quality surfaces compared to StreetSurf and MVS methods. MVS-generated meshes have noisy normals and are incomplete. We observe that our method recovers more accurate and realistic scene details in many regions such as buildings, cars, poles, and trees. Our analysis supports the hypothesis that StreetSurf’s disentanglement of the close and far range based on the assumption that driving scenes are long and narrow is not adapted to the majority of driving sequences. In addition, StreetSurf’s road-surface initialization fails in sequences where the road and sidewalks are not at the same height or at non-flat roads such as downhill (see Fig. 8 – Seq. 30).

4.6. Ablation study

Convergence of density field compared to SDF field. We report in Fig. 6a the Chamfer Distance between LiDAR and predicted point clouds, for Seq. 31 from KITTI-360 and Seq. 916 from nuScenes, comparing two different NeRF: one solely based on density volumetric field and another one solely based on SDF at various training steps (without normal supervision, as we cannot supervise normal in case of pure density volumetric field). The results support the claim that density field converges faster compared to the SDF field.

SCILLA’s components. In this section, we ablate SCILLA’s SDF progressive initialization strategy, with quantitative results reported in Tab. 3. The results confirm that transitioning from volumetric to surface representation is essential for accurately initializing the SDF field and efficiently reconstructing driving sequences. We also report results with standard accumulated normal supervision and without network regularization loss.

Hybrid stage duration. To evaluate our progressive ini-

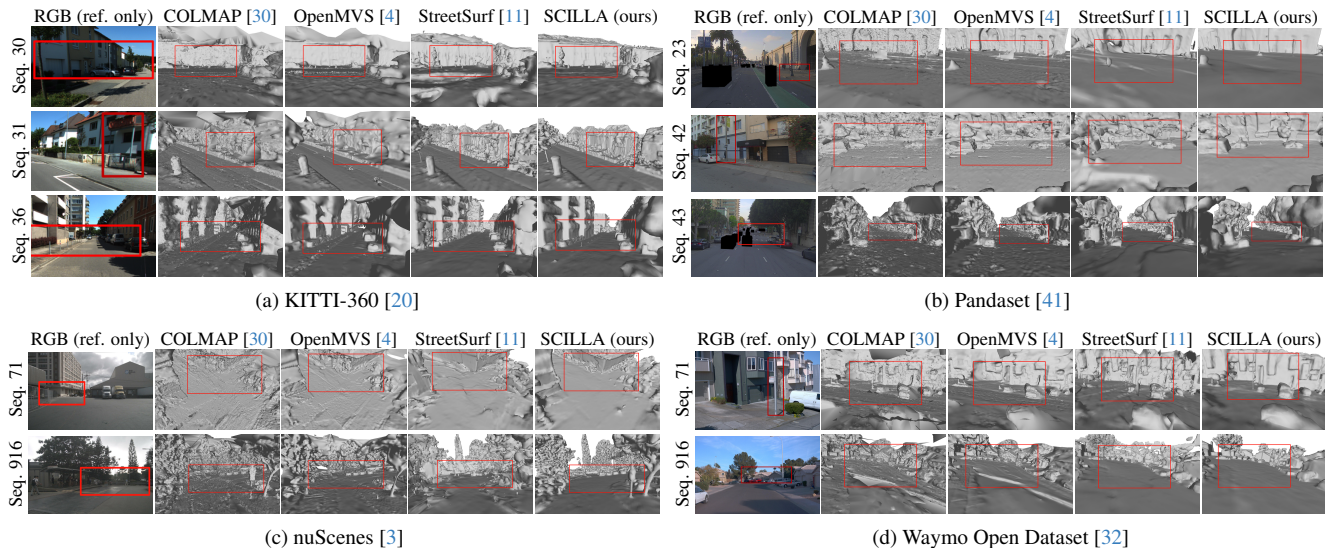


Figure 5. Qualitative experiments results on (a) KITTI-360s [20], (b) Pandaset [41], (c) nuScenes [3] and (d) Waymo Open Dataset [32]. RGB ground-truth images shown for reference of the scene layout. Complex scene geometries reconstructed in the mesh are highlighted in red squares. We compare our generated SDF mesh to COLMAP, OpenMVS and StreetSurf [11] meshes.

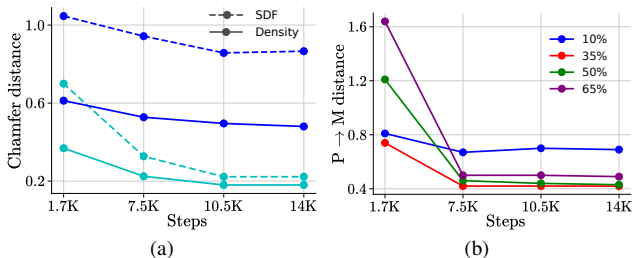


Figure 6. (a) Chamfer distance between LiDAR and predicted point cloud of Density field and SDF field at different training steps, for nuScenes and KITTI-360. (b) P→M for different hybrid stage duration at different training steps for Seq. 23 from Pandaset.

Table 3. Ablations study: we deactivate some SCILLA’s key components. (a) without progressive initialization (b) with the accumulated normal for $\mathcal{L}_{\hat{N}}$ (c) without \mathcal{L}_s .

Seq.	w/o SDF init		w/o $\mathcal{L}_{\hat{N}}$		w/o \mathcal{L}_s		SCILLA	
	P→M	Prec.	P→M	Prec.	P→M	Prec.	P→M	Prec.
KITTI-360. 31	0.35	0.18	0.19	0.27	0.24	0.15	0.15	0.71
Pandaset. 23	0.85	0.18	0.80	0.18	0.54	0.17	0.51	0.23
nuScenes. 0916	0.35	0.4	0.4	0.21	0.35	0.15	0.25	0.54
Waymo. 10061	0.3	0.36	0.22	0.32	0.34	0.17	0.23	0.43

tialization approach, we report the P→M distance at various iterations with different transition times in Fig. 6b. The results show that a short hybrid stage is insufficient for proper SDF field initialization, while an extended hybrid stage leads to losing SDF field initialization, resulting in suboptimal reconstructions.

5. Discussion

Applications. Thanks to the quality and completeness of SCILLA’s reconstructed meshes, we can use modern MVS tools such as OpenMVS [4] to obtain a detailed and colored representation of large urban scenes, as shown in Fig. 1. In addition, SCILLA is not restricted to driving scenarios, it can be applied to other types of scenes. We encourage the reader to refer to the supplementary materials for qualitative results of SCILLA on the Tanks&Temples dataset [18].

Limitations. Although our method can achieve highly detailed surface reconstruction in driving scenarios, it fails to reconstruct fine details in very wide and open sequences. We recommend consulting the supplementary materials for the failure cases of SCILLA.

6. Conclusion

In this work we presented **SCILLA**, an implicit hybrid approach to efficiently reconstruct large urban scenes. Our method’s hybrid architecture models the volumetric density and signed distance in two separate fields. We introduced a novel hybrid volume rendering strategy to progressively transition from volumetric representation to a signed distance representation. The quantitative and qualitative evaluations that we performed show that SCILLA achieves more precise reconstruction than state-of-the-art methods while being significantly faster and is better suited for a large variation of driving scenarios.

SCILLA: SurfaCe Implicit Learning for Large urban Area, a volumetric hybrid solution

Supplementary Material

In this supplementary material, we provide additional implementation details, experiments with Neuralangelo [19], additional qualitative results, ablation study on our samples attribution strategy, applications, and failure cases of SCILLA.

7. SDF-gradient normalization

As introduced in Sec. 3.3 of the main paper, volumetric representations based on density estimation tend to quickly approximate saturated alpha values (α_i^v being either 0 or 1), while alpha values computed from the SDF converge slower. Because α_i^v and α_i^f are composed jointly during the hybrid stage, we noticed that surface representation compensates for this gap by predicting large SDF gradient values so that α_i^f aligns with α_i^v . Indeed, from Eq. 3 of the main paper, a solution to saturate alpha towards either 1 or 0, is to predict $f(p_{i+1}) \ll f(p_i)$ or $f(p_{i+1}) \gg f(p_i)$, respectively. During the forward pass, $f(p_i)$ and $f(p_{i+1})$ are not directly predicted by the model but rather computed using:

$$\begin{aligned} f(p_i) &= f(x_i) + \text{Relu}(-\cos(\theta)) \times \frac{\delta_i}{2}, \\ f(p_{i+1}) &= f(x_i) - \text{Relu}(-\cos(\theta)) \times \frac{\delta_i}{2}, \end{aligned} \quad (9)$$

with θ being the angle between the direction of $\nabla f(x_i)$ and the ray direction d . Practically, we do not formally compute θ but we rather approximate its cosine with $\cos(\theta) = \nabla f(x_i) \cdot d$, **assuming both vectors are unit norm**. By predicting $\|\nabla f(x_i)\|_2 \gg 1$, α_i^f can be easily saturated and follow the distribution of α_i^v without learning a proper signed distance field. To address this, we simply normalize the SDF gradient before the cosine computation to prevent the gradient from compensating the alpha distribution difference. It is important to notice that even if the eikonal loss used for training (see main paper) is supposed to encourage the network to model a signed distance function with spatial derivative of unitary norm, we found that numerically normalizing the gradient during our hybrid stage is essential to avoid divergence in early training iterations.

8. SDF Field Initialization: Neuralangelo

As detailed in the main paper, Neuralangelo [19] is designed for landmark reconstruction, relying on many overlapping images and a bounded region of interest to initialize the SDF with a spherical shape. In our initial tests, when apply-

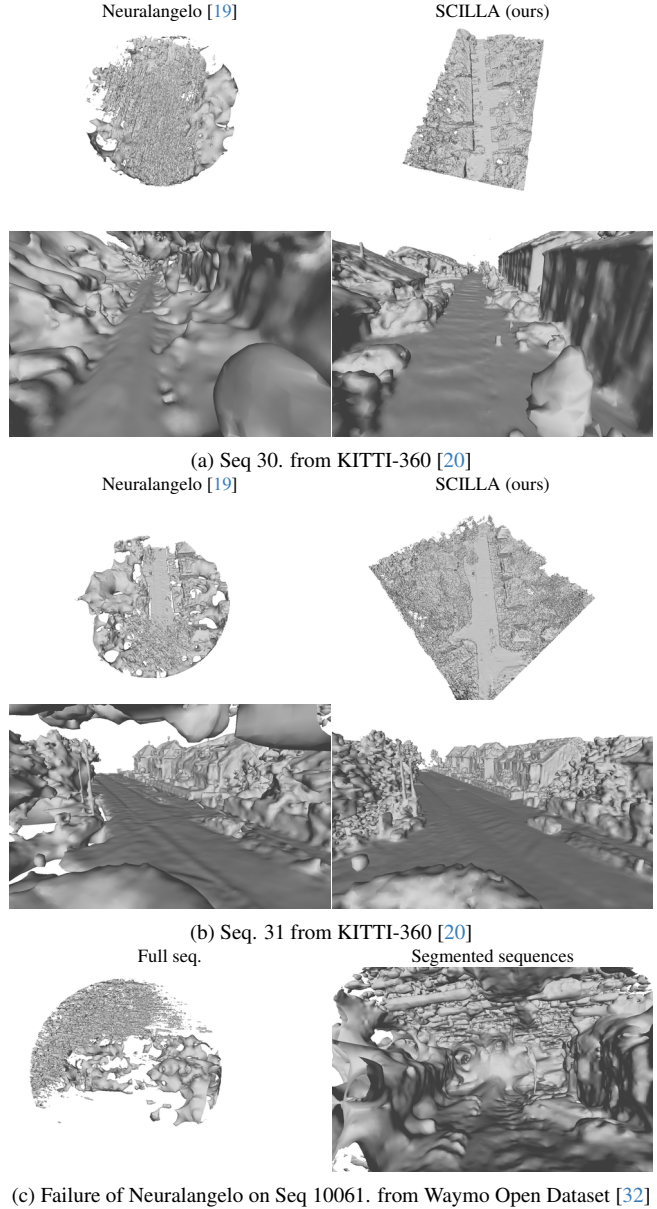


Figure 7. Qualitative experiments results on Seq. 30 (a) and Seq. 31 (b) from KITTI-360s [20]. Failure on Seq. 10061 (c) Waymo Open Dataset [32]. We compare our generated SDF mesh to Neuralangelo [19] mesh for KITTI-360. We report the experiments on the full and segmented sequence for Waymo.

ing Neuralangelo (using the official authors codebase ¹) to

¹<https://github.com/NVlabs/neuralangelo>

outdoor driving scenarios using the default settings for outdoor scenes, we observed that the initial part of the scene remained noisy and retained a spherical shape. Only the final part of the scene, which was consistently visible across all images in the sequence, was accurately reconstructed (see Fig. 7a). While Neuralangelo managed to reconstruct some parts of simpler scenes, such as in Seq. 31 from KITTI-360 (Fig. 7b), it failed completely in more complex cases, particularly in sequences that are long, wide, or contain challenging structure like downhill (e.g., Seq. 30 in Fig. 7a). Moreover, Neuralangelo was unable to reconstruct any part of the Waymo dataset, as shown in Fig. 7c. Given these outcomes, we conducted extensive experiments with Neuralangelo using various training strategies:

- Constraining the spherical shape: since Neuralangelo relies on a spherical initialization where everything outside the sphere is treated as background, we attempted to center the sphere on a smaller region, with a smaller radius. However, this approach resulted in very noisy reconstructions, likely due to insufficient overlapping images in that part of the scene (inside the sphere).
- Segmenting the scene into multiple parts: acknowledging that driving sequences are typically long and wide, we divided the scenes into smaller segments to better fit the spherical initialization. This strategy, however, produced unsatisfactory results. Neuralangelo requires a large number of images (typically 300 for an average Tanks and Temples scene covering the same region of interest) while KITTI-360 sequences contain around 200 images (approximately 50 per camera) and after segmentation, each part of the scene had roughly 100 images. The method could only reconstruct the final segment of the scene that was visible in all images (see Fig. 7c).
- Doubling the number of images: we further experimented with doubling the number of images used in the reconstruction. Unfortunately, this did not help the method to converge to a satisfactory reconstruction.

Despite various training strategies, Neuralangelo failed to produce reliable reconstructions for complex driving sequences. It requires a large number of overlapping images and a tightly bounded scene, making it unsuitable for unbounded driving sequences. Additionally, Neuralangelo’s training time is prohibitively long, taking up to 24 hours per scene. This, combined with its poor performance on driving sequences, makes it impractical for large-scale driving scene reconstruction tasks.

9. Additional implementation details

We use the poses provided by the datasets, except for Waymo, where we recompute the vehicle trajectory and sensor calibration with MOISST [13] due to inaccuracies in the provided data. The overall loss we use to optimize

Table 4. Hash grid encoding parameters

Parameter	Value
Table size	2^{19}
Finest resolution	2048
Coarsest resolution	16
Number of level	16

Table 5. Selected KITTI-360 sequences

Seq.	KITTI Sync.	Start	End	# frames per cam.
30	0004	1728	1822	48
31	0009	2890	2996	54
35	0009	980	1092	57
36	0010	112	166	28

SCILLA is defined as follows:

$$\mathcal{L} = \mathcal{L}_{\text{rgb}} + \lambda_1 \mathcal{L}_{\text{dssim}} + \lambda_2 \mathcal{L}_{\hat{N}} + \lambda_3 \mathcal{L}_{\text{eik}} + \lambda_4 \mathcal{L}_{\text{sky}}. \quad (10)$$

We set λ_1 , and λ_4 to 0.1 and 0.01, respectively. We fix λ_2 to 0.05 for planar classes and 0.01 for non planar classes. We set λ_3 to 0.01 in the first training iterations, then we adjust it to 0.1 in the last iterations.

We report in table 4 the hash grid encoding parameters from Instant-NGP [25]. We summarize the split of KITTI-360 [20] sequences used for our evaluations in table 5. We use all four cameras for KITTI-360 [20], and the three front cameras for Pandaset [41], nuScenes [3] and Waymo Open Dataset [32]. We sample one image out of two for KITTI-360, and one image out of 8 for the other datasets.

10. Additional results

10.1. Additional qualitative results

We report in Fig. 8 additional qualitative results on nuScenes [3] and Waymo Open Dataset [32]. We find that SCILLA reconstructs higher-quality surfaces compared to StreetSurf and can recover many scene details (see highlighted red-boxes on the figures).

10.2. Ablation study

We ablate the effect of random sample attribution and our proposed probability-based samples attribution. The qualitative results at various training steps are presented in Fig. 9. The results demonstrate that SCILLA samples attribution strategy initially learns the coarse geometry of the scene during early training stages. While random sample attribution can approximate an accurate SDF representation by the end of the hybrid stage, it results in an incomplete mesh compared to the mesh generated using probability-based sample attribution.

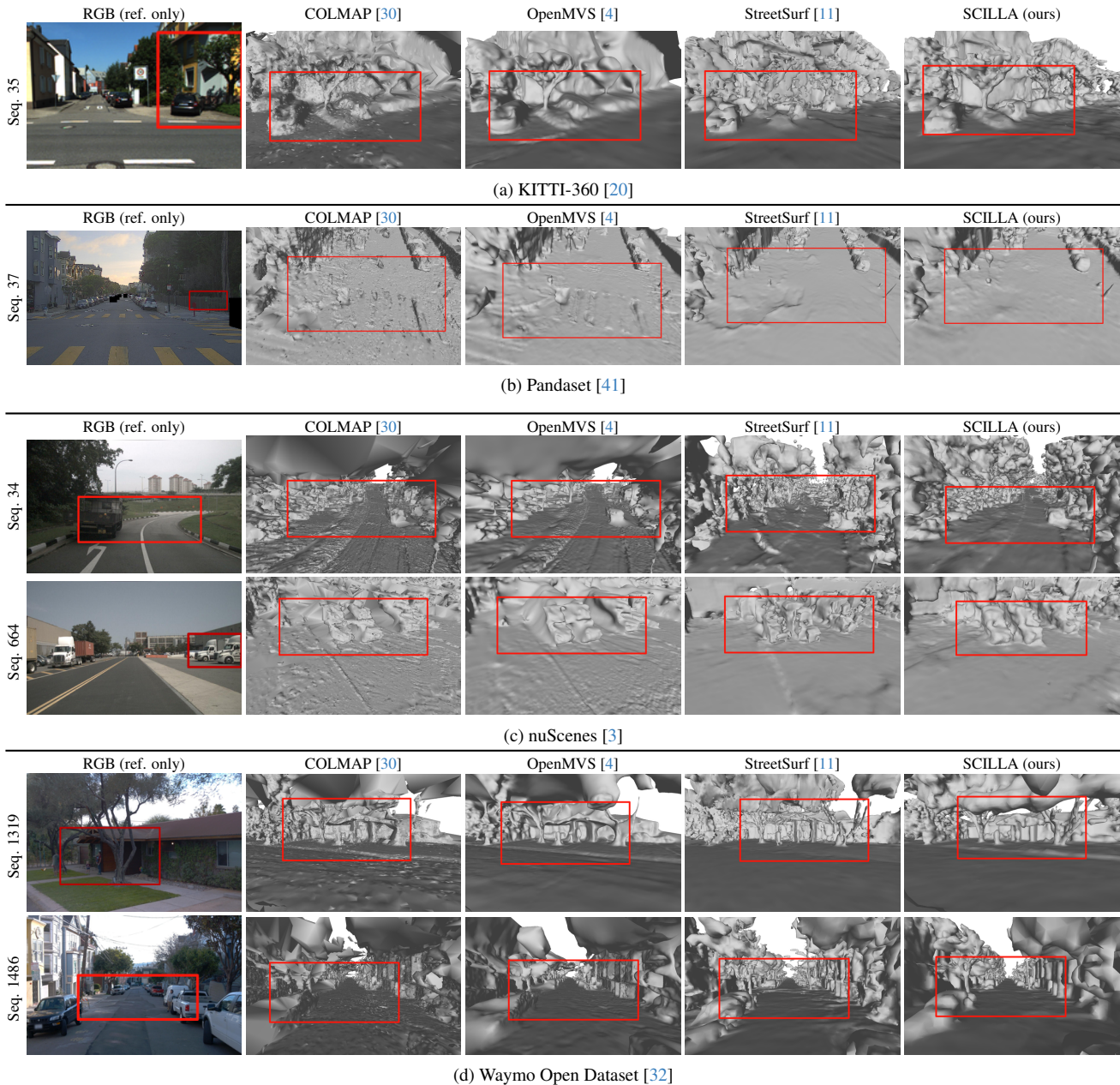


Figure 8. Qualitative experiments results on (a) KITTI-360s [20], (b) Pandaset [41], (c) nuScenes [3] and (d) Waymo Open Dataset [32]. RGB ground-truth images shown for reference of the scene layout. Complex scene geometries reconstructed in the mesh are highlighted in red squares. We compare our generated SDF mesh to COLMAP, OpenMVS and StreetSurf [11] meshes.

11. Applications

11.1. Tanks And Temples dataset

In this section, we report SCILLA’s qualitative results on Tanks and Temples dataset [18]. The results reported in Fig. 10 demonstrate that SCILLA is not restricted to driving datasets and urban areas. SCILLA can represent large, detailed, indoor and outdoor sequences from Tanks And

Temples. We report the results of SCILLA with and without the hybrid volumetric stages. Our observation suggests that the transition from the volumetric to surface representation enables to recover various scene details. In addition, SCILLA’s training time takes less than an hour, compared to other state-of-the-art indoor and outdoor landmarks reconstruction methods, such as Neuralangelo [19] which requires 24h of training.

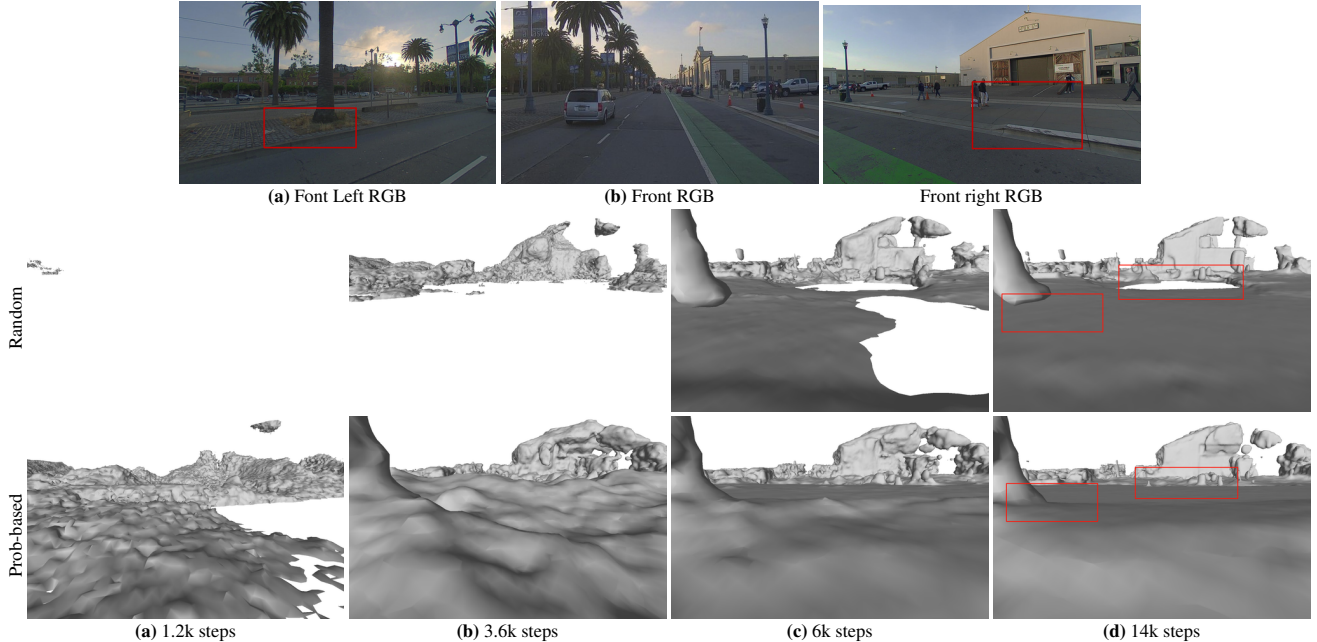


Figure 9. Ablation study: we ablate the effect of random samples attribution compared to our probability-guided attribution introduced in section 3.3 of the paper. We show the rendered meshes results of the sequence 023 of Pandaset [41] at (a) 1.2k steps, (b) 3.6k steps, (c) 6k steps, and (d) 14k steps.

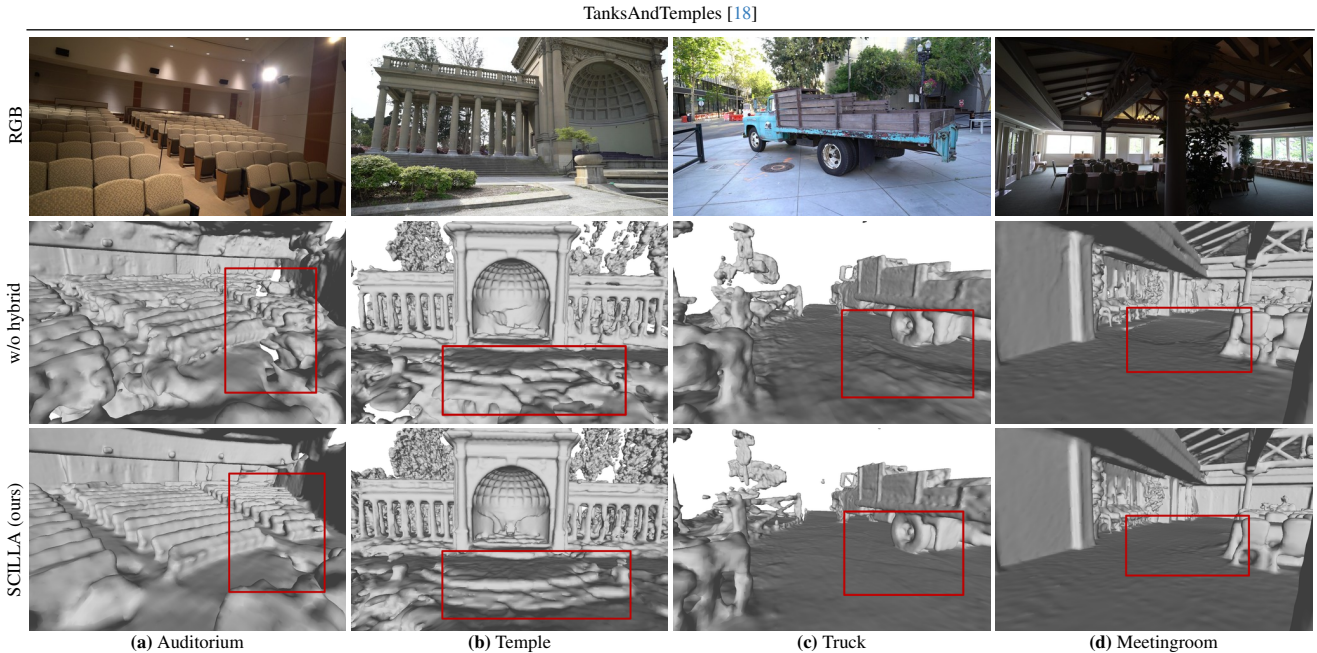


Figure 10. Qualitative experiments on TanksAndTemples dataset [18]. We report the RGB ground-truth image. In a different point-of-view than the GT RGB, we compare the extracted mesh from the SDF from both SCILLA, and SCILLA without the hybrid stages.

11.2. Textured mesh

Due to the high-quality of SCILLA’s reconstructed surfaces, we can leverage modern Multi-View Stereo (MVS) tools

like OpenMVS [4] to produce detailed and colored representations of driving sequences. As shown in Fig. 11, we find that SCILLA’s textured mesh is more complete and accurate compared to StreetSurf’s textured mesh.



Figure 11. We use OpenMVS [4] to assign texture to the outputted meshes. We compare our colored mesh to StreetSurf [11], for the sequence 102751 from Waymo Open Dataset [32].

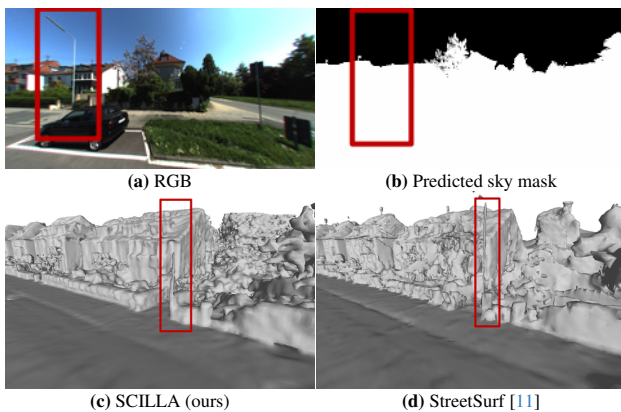


Figure 12. Failure case of SCILLA for the sequence 31 from KITTI-360 [20]. We report the ground-truth RGB image and the predicted sky mask. In a different point-of-view than the GT RGB, we compare our generated SDF mesh to StreetSurf’s mesh.

12. Limitations

Although SCILLA’s reconstructed surfaces are highly detailed and accurate, we find that our method can fail in three distinct scenarios:

- Disentangling fine details from the sky: unlike StreetSurf [11], which models close range, far range, and sky separately, SCILLA separates only the sky from the other scene’s modeling. However, SCILLA may struggle to

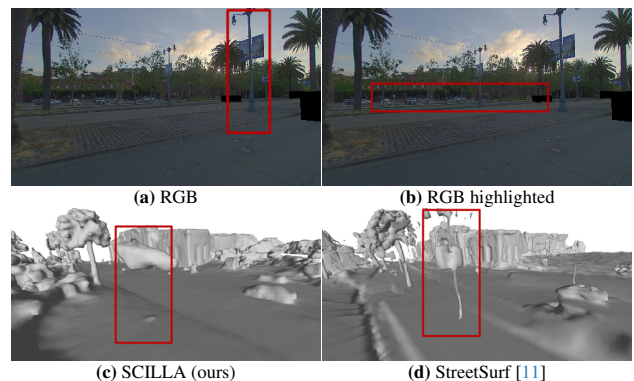


Figure 13. Failure case of SCILLA for the sequence 23 from Pandaset [41]. We report the ground-truth RGB image and the wide part of the sequence highlighted. In a different point-of-view than the GT RGB, we compare our generated SDF mesh to StreetSurf’s mesh.

distinguish fine details from the sky, particularly in cases where objects are thin, as shown in Fig. 12.

- Fine details in wide sequences: SCILLA sometimes fails in accurately reconstructing scene details in wide and open sequences, such as scene 23 from Pandaset reported in Fig. 13.
- Inaccurate road reconstruction: for sequence 664 from nuScenes (see Fig. 14), SCILLA faces challenges in re-

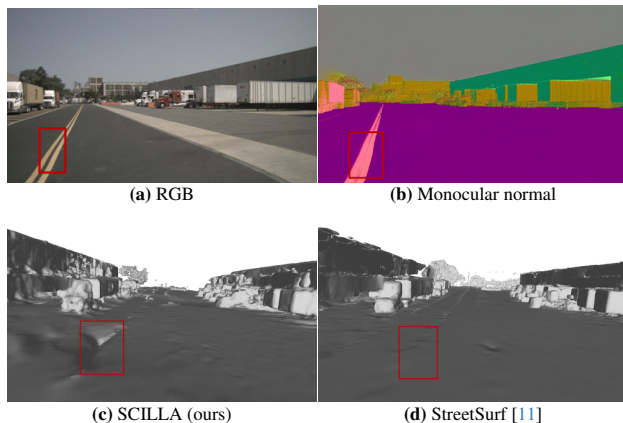


Figure 14. Failure case of SCILLA for the sequence 664 from nuScenes [3]. We report the ground-truth RGB image and the monocular normal. In a different point-of-view than the GT RGB we compare our generated SDF mesh to StreetSurf’s mesh.

constructing the road due to inaccuracies in the monocular normal prediction from Omnidata [8]. In comparison, StreetSurf [11] demonstrates more accurate road reconstruction, attributed to its road-surface initialization.

References

- [1] Jonathan T. Barron, Ben Mildenhall, Dor Verbin, Pratul P. Srinivasan, and Peter Hedman. Mip-nerf 360: Unbounded anti-aliased neural radiance fields. In *CVPR*, 2022. 4
- [2] Matthew Berger, Andrea Tagliasacchi, Lee M. Seversky, Pierre Alliez, Gaël Guennebaud, Joshua A. Levine, Andrei Sharf, and Cláudio T. Silva. A survey of surface reconstruction from point clouds. *Computer Graphics Forum*, 36, 2017. 2
- [3] Holger Caesar, Varun Bankiti, Alex H. Lang, Sourabh Vora, Venice Erin Liong, Qiang Xu, Anush Krishnan, Yu Pan, Giancarlo Baldan, and Oscar Beijbom. nuscenes: A multi-modal dataset for autonomous driving. In *CVPR*, 2020. 2, 6, 8, 3
- [4] Dan Cernea. OpenMVS: Multi-view stereo reconstruction library. 2020. 6, 7, 8, 3, 4, 5
- [5] Hanlin Chen, Chen Li, and Gim Hee Lee. Neusg: Neural implicit surface reconstruction with 3d gaussian splatting guidance, 2023. 3
- [6] Bowen Cheng, Ishan Misra, Alexander G. Schwing, Alexander Kirillov, and Rohit Girdhar. Masked-attention mask transformer for universal image segmentation. In *CVPR*, 2022. 5
- [7] Jeremy S De Bonet and Paul Viola. Poxels: Probabilistic voxelized volume reconstruction. In *ICCV*, 1999. 2
- [8] Ainaz Eftekhari, Alexander Sax, Jitendra Malik, and Amir Zamir. Omnidata: A scalable pipeline for making multi-task mid-level vision datasets from 3d scans. In *ICCV*, 2021. 2, 6
- [9] Silvano Galliani, Katrin Lasinger, and Konrad Schindler. Gipuma: Massively parallel multi-view stereo reconstruction. In *ICCV*, 2016. 2
- [10] Amos Gropp, Lior Yariv, Niv Haim, Matan Atzmon, and Yaron Lipman. Implicit geometric regularization for learning shapes. In *MLSYS*, 2020. 5
- [11] Jianfei Guo, Nianchen Deng, Xinyang Li, Yeqi Bai, Botian Shi, Chiyu Wang, Chenjing Ding, Dongliang Wang, and Yikang Li. Streetsurf: Extending multi-view implicit surface reconstruction to street views, 2023. 1, 2, 3, 5, 6, 7, 8
- [12] Yuan-Chen Guo, Yan-Pei Cao, Chen Wang, Yu He, Ying Shan, Xiaohu Qie, and Song-Hai Zhang. Vmesh: Hybrid volume-mesh representation for efficient view synthesis, 2023. 3
- [13] Quentin Herau, Nathan Piasco, Moussab Bennehar, Luis Roldão, Dzmitry Tsishkou, Cyrille Migniot, Pascal Vasseur, and Cédric Demonceaux. Moisst: Multimodal optimization of implicit scene for spatiotemporal calibration. In *IROS*. IEEE, 2023. 2
- [14] Zhangjin Huang, Zhihao Liang, Haojie Zhang, Yangkai Lin, and Kui Jia. Sur2f: A hybrid representation for high-quality and efficient surface reconstruction from multi-view images, 2024. 3
- [15] Michal Jancosek and Tomáš Pajdla. Exploiting visibility information in surface reconstruction to preserve weakly supported surfaces. *International Scholarly Research Notices*, 2014, 2014. 7
- [16] Michael Kazhdan, Matthew Bolitho, and Hugues Hoppe. Poisson surface reconstruction. In *Eurographics Symp. Geometry Processing*, page 61–70, 2006. 2
- [17] Bernhard Kerbl, Georgios Kopanas, Thomas Leimkühler, and George Drettakis. 3d gaussian splatting for real-time radiance field rendering. *ACM Transactions on Graphics*, 42(4), 2023. 3
- [18] Arno Knapitsch, Jaesik Park, Qian-Yi Zhou, and Vladlen Koltun. Tanks and temples: Benchmarking large-scale scene reconstruction. *ACM Transactions on Graphics*, 36(4), 2017. 8, 3, 4
- [19] Zhaoshuo Li, Thomas Müller, Alex Evans, Russell H Taylor, Mathias Unberath, Ming-Yu Liu, and Chen-Hsuan Lin. Neuralangelo: High-fidelity neural surface reconstruction. In *CVPR*, 2023. 2, 3, 6, 1
- [20] Yiyi Liao, Jun Xie, and Andreas Geiger. KITTI-360: A novel dataset and benchmarks for urban scene understanding in 2d and 3d. *PAMI*, 2022. 2, 6, 8, 1, 3, 5
- [21] William E. Lorensen and Harvey E. Cline. Marching cubes: A high resolution 3d surface construction algorithm. 21(4), 1987. 6
- [22] Charles Malleon, Jean-Yves Guillemaut, and Adrian Hilton. 3d reconstruction from rgb-d data. *RGB-D Image Analysis and Processing*. 2
- [23] Ben Mildenhall, Pratul P. Srinivasan, Matthew Tancik, Jonathan T. Barron, Ravi Ramamoorthi, and Ren Ng. Nerf: Representing scenes as neural radiance fields for view synthesis. In *ECCV*, 2020. 1, 2, 3
- [24] Pierre Moulon, Pascal Monasse, Romuald Perrot, and Renaud Marlet. OpenMVG: Open multiple view geometry. In *International Workshop on Reproducible Research in Pattern Recognition*, pages 60–74. Springer, 2016. 2

- [25] Thomas Müller, Alex Evans, Christoph Schied, and Alexander Keller. Instant neural graphics primitives with a multi-resolution hash encoding. *ACM Trans. Graph.*, 41(4):102:1–102:15, 2022. 6, 2
- [26] Despoina Paschalidou, Ali Osman Ulusoy, Carolin Schmitt, Luc van Gool, and Andreas Geiger. Raynet: Learning volumetric 3d reconstruction with ray potentials. In *CVPR*, 2019. 2
- [27] Konstantinos Rematas, Andrew Liu, Pratul P. Srinivasan, Jonathan T. Barron, Andrea Tagliasacchi, Tom Funkhouser, and Vittorio Ferrari. Urban radiance fields. In *CVPR*, 2022. 2, 3
- [28] Luis Roldão, Raoul de Charette, and Anne Verroust-Blondet. 3d surface reconstruction from voxel-based lidar data. (*ITSC*), pages 2681–2686, 2019. 2
- [29] Johannes L Schönberger, Enliang Zheng, Jan-Michael Frahm, and Marc Pollefeys. Pixelwise view selection for unstructured multi-view stereo. In *ECCV*, pages 501–518, 2016. 2
- [30] Johannes Lutz Schönberger, Enliang Zheng, Marc Pollefeys, and Jan-Michael Frahm. Pixelwise view selection for unstructured multi-view stereo. In *ECCV*, 2016. 6, 7, 8, 3
- [31] Robust Multiview Stereopsis. Accurate, dense, and robust multiview stereopsis. *TPAMI*, 32(8):1362–1376, 2010. 2
- [32] Pei Sun, Henrik Kretschmar, Xerxes Dotiwalla, Aurelien Chouard, Vijaysai Patnaik, Paul Tsui, James Guo, Yin Zhou, Yuning Chai, Benjamin Caine, Vijay Vasudevan, Wei Han, Jiquan Ngiam, Hang Zhao, Aleksei Timofeev, Scott Ettinger, Maxim Krivokon, Amy Gao, Aditya Joshi, Yu Zhang, Jonathon Shlens, Zhifeng Chen, and Dragomir Anguelov. Scalability in perception for autonomous driving: Waymo open dataset. In *CVPR*, 2020. 2, 3, 6, 8, 1, 5
- [33] Jiaxiang Tang, Hang Zhou, Xiaokang Chen, Tianshu Hu, Errui Ding, Jingdong Wang, and Gang Zeng. Delicate textured mesh recovery from nerf via adaptive surface refinement. In *ICCV*, 2023. 3
- [34] Shubham Tulsiani, Tinghui Zhou, Alexei A. Efros, and Jitendra Malik. Multi-view supervision for single-view reconstruction via differentiable ray consistency. In *CVPR*, 2017. 2
- [35] Ali Osman Ulusoy, Andreas Geiger, and Michael J. Black. Towards probabilistic volumetric reconstruction using ray potentials. In *3DV*, 2015. 2
- [36] Fusang Wang, Arnaud Louys, Nathan Piasco, Moussab Bennehar, Luis Roldão, and Dzmity Tsishkou. Planerf: Svd unsupervised 3d plane regularization for nerf large-scale urban scene reconstruction. In *3DV*, 2024. 5
- [37] Peng Wang, Lingjie Liu, Yuan Liu, Christian Theobalt, Taku Komura, and Wenping Wang. Neus: Learning neural implicit surfaces by volume rendering for multi-view reconstruction. In *NeurIPS*, 2021. 1, 2, 3, 5
- [38] Yiming Wang, Qin Han, Marc Habermann, Kostas Daniilidis, Christian Theobalt, and Lingjie Liu. Neus2: Fast learning of neural implicit surfaces for multi-view reconstruction. In *ICCV*, 2023. 2
- [39] Zian Wang, Tianchang Shen, Jun Gao, Shengyu Huang, Jacob Munkberg, Jon Hasselgren, Zan Gojcic, Wenzheng Chen, and Sanja Fidler. Neural fields meet explicit geometric representation for inverse rendering of urban scenes. In *CVPR*, 2023. 1, 2, 3
- [40] Zian Wang, Tianchang Shen, Merlin Nimier-David, Nicholas Sharp, Jun Gao, Alexander Keller, Sanja Fidler, Thomas Müller, and Zan Gojcic. Adaptive shells for efficient neural radiance field rendering. In *SIGGRAPH Asia*, 2023. 3
- [41] Pengchuan Xiao, Zhenlei Shao, Steven Hao, Zishuo Zhang, Xiaolin Chai, Judy Jiao, Zesong Li, Jian Wu, Kai Sun, Kun Jiang, et al. Pandaset: Advanced sensor suite dataset for autonomous driving. In *ITSC*, 2021. 2, 6, 8, 3, 4, 5
- [42] Lior Yariv, Jiatao Gu, Yoni Kasten, and Yaron Lipman. Volume rendering of neural implicit surfaces. In *NeurIPS*, 2021. 1, 2
- [43] Zehao Yu, Songyou Peng, Michael Niemeyer, Torsten Sattler, and Andreas Geiger. Monosdf: Exploring monocular geometric cues for neural implicit surface reconstruction. *NeurIPS*, 2022. 2, 5
- [44] Jingyang Zhang, Yao Yao, Shiwei Li, Jingbo Liu, Tian Fang, David McKinnon, Yanghai Tsin, and Long Quan. Neif++: Inter-reflectable light fields for geometry and material estimation. In *ICCV*, 2023. 1
- [45] Jingsen Zhu, Yuchi Huo, Qi Ye, Fujun Luan, Jifan Li, Dianbing Xi, Lisha Wang, Rui Tang, Wei Hua, Hujun Bao, and Rui Wang. I2-sdf: Intrinsic indoor scene reconstruction and editing via raytracing in neural sdf. In *CVPR*, 2023. 1
- [46] Michael Zollhöfer, Patrick Stotko, Andreas Görlitz, Christian Theobalt, Matthias Nießner, R. Klein, and Andreas Kolb. State of the art on 3d reconstruction with rgb-d cameras. *Computer Graphics Forum*, 37, 2018. 2